Effects of Annealing Temperature on the Performance of Organic Solar Cells Based on Polymer: Non-Fullerene Using V₂O₅ as HTL

JOSÉ G. SÁNCHEZ [1], **ALFONSINA A. A. TORIMTUBUN**[1], **VÍCTOR S. BALDERRAMA**[2] (Member, IEEE),
MAGALI ESTRADA[3] (Senior Member, IEEE), **JOSEP PALLARÈS**[1] (Senior Member, IEEE),
AND LLUIS F. MARSAL [1] (Senior Member, IEEE)

1 Departament d'Enginyeria Electronica Electrica i Automatica, Universitat Rovira i Virgili, 43007 Tarragona, Spain
2 Cátedra-CONACYT, Mictrotecnologías, Centro de Ingeniería y Desarrollo Industrial, Santiago de Querétaro 76125, Mexico
3 Sección de Electrónica del Estado Sólido, Departamento de Ingeniería Eléctrica, CINVESTAV, Mexico City 07360, Mexico

CORRESPONDING AUTHOR: L. F. MARSAL (e-mail:lluis.marsal@urv.cat)

ABSTRACT The annealing temperature and thickness are two important factors to optimize the morphology of the active layer for a better performance of inverted polymer solar cells (iPSCs). Herein, the effects of the annealing temperature and the thickness of the active layer on the performances of iPSCs based on PBDB-T:IT-M are analyzed. Titanium oxide and vanadium oxide are used as electron and hole transporting layers, respectively. The device made with PBDB-T:IT-M layer (ca. 90 nm thick) thermally annealed at 100 °C exhibits the best performing under simulated AM 1.5G light. The idealities factor of iPSCs with two different annealing temperatures are determined by measuring the open-circuit voltage as a function of light intensity. The study shows that recombination losses in iPSCs annealed at 160 °C are governed by non-geminate recombination mechanisms, while in iPSCs annealed at 100 °C, the recombination losses are mainly due to band-tail trap states. Additional impedance spectroscopy measurements reveal that the device with an annealing temperature of 160 °C exhibits a higher charge-transfer in the bulk layer. However, the device thermally annealed at 100 °C shows lower charge-transfer resistance through all layers involved in the charge extraction. The results of this work show the importance of the annealing temperature on the charge-transfer at the active layer/vanadium oxide interface.

INDEX TERMS PBDB-T:IT-M, iPSCs, impedance spectroscopy, recombination mechanism, titanium oxide, non-fullerene acceptors.

I. INTRODUCTION

Polymer-based solar cells (PSCs) with a bulk heterojunction (BHJ) structure are considered as a good energy source in the renewable energy field because they offer the opportunity to fabricated lightweight and transparent devices on flexible substrates with large areas at low manufacturing cost [1]–[3]. In the last years, main efforts were focused on the development of novel electron-donating polymers with low band gaps and an enhanced spectral coverage [4], [5]. Typically, a thin film of metal calcium (Ca) is used

as the electron-transporting layer (ETL), and the conductive polymer poly(3,4-ethylenedioxythiophene):poly (styrenesulfonate) (PEDOT:PSS) is used as a hole-transporting layer in conventional PSCs [6]–[8]. However, the strongly oxidizing properties of Ca and the hygroscopic nature of PEDOT:PSS limit the performance and lifetime of PSCs [9]–[12]. Therefore, the Ca is replaced by titanium oxide (TiOₓ) [13]–[15], zinc oxide (ZnO) [16], [17], and the poly[(9,9-bis(3-(N,N-dimethylamino) propyl)-2,7-fluorene)-alt-2,7-(9,9 dioctylfluorene)] (PFN) [18], [19], as electron

transporting layer (ETL) due to their high transparency as thin films and good electron mobility, moreover they can modify the surface of indium tin oxide (ITO) in order to improve the electron collection efficiency. Therefore, PEDOT:PSS is mainly replaced by metal oxides such as molybdenum oxide (MoO_3), nickel oxide (NiO), or vanadium oxide (V_2O_5) since they can provide a low resistance ohmic at the HTL/bulk interface and increase the stability of devices [20]. Moreover, the morphology of the active layer is another critical factor for achieving high efficiencies, since the charge-separation and charge-transporting depend on the interface and the interpenetrated networks of the bulk. The active layer morphology is commonly controlled by solvents, additives, and annealing treatments.

Organic solar cells based on electron-donating polymers and electron-accepting fullerenes with high efficiencies, e.g., PTB7:PC$_{70}$ BM [13], [18], PTB7-Th:PC$_{70}$ BM [14], [19], [21], has been reported. Although encouraging efficiencies have been obtained with PSCs based on polymer-fullerene [19], [21], the performance of devices is limited by fullerenes properties such as weak light absorption in the visible region, poor ambient stability, monotonous tunability of molecular energy levels, and a high electron affinity which limits the V_{OC} of the devices [22]. Currently, non-fullerenes electron-acceptors (NFAs) are considered as promise materials to replace the fullerenes acceptor since they offer higher thermal stability, broader optical absorption properties, facile tunable molecular energy levels, and lower-cost synthesis than those of fullerenes acceptors [22], [23]. Amongst the different NFAs reported [24]–[26], the 3,9-bis(2-methylene-(3-(1,1dicyanomethylene)-indanone))-5,5,11,11-tetrakis(4hexyl phenyl)-dithieno[2,3d:2',3'd']-s-indaceno[1,2-b:5,6-b']dithio phene (so-called ITIC) and its derivatives (IT-M, IT-Th, IT-F, IT-4F, to mention some) are low bandgap NF-Acceptors widely used in the fabrication of high-efficiency polymer solar cells [27]–[31]. Several authors have reported PSCs with efficiencies over 10% based on IT-M blended with the medium-bandgap and semicrystalline polymer Poly[(2,6-(4,8-bis(5-(2-ethylhexyl)thiophen-2-yl)-benzo[1,2-b:4,5-b']dithiophene)) alt-(5,5-(1',3'-di-2-thienyl-5',7'-bis(2-ethylhexyl)benzo[1',2' c:4',5'-c']dithiophene-4,8-dione)] (namely PBDB-T). Those high efficiencies were reached by using inverted structures, where MoO_3 was commonly used as HTL, while ZnO and TiO_2 were used as the ETL [28], [32]–[34].

In this work, we report on the fabrication and electrical characterization of iPSCs based on the low-bandgap non-fullerene acceptor IT-M, and PBDB-T. The PSCs were fabricated using a thin film of TiO_x as the ETL and ITO as the cathode. On the other hand, we used V_2O_5 as a better cost-effective HTL in comparison to the MoO_3. Finally, silver (Ag) was used as the top-contact anode. The structure of iPSC is ITO/TiO_x/PBDB-T:IT-M/V_2O_5/Ag. We analyzed the effects of the PBDB-T:IT-M layer thickness, and annealing temperature on the performance of devices by measuring the

typical current density–voltage (*J-V*) characteristics under simulated illumination. The losses due to the recombination mechanism and the interfacial resistances were also analyzed.

II. EXPERIMENTAL AND METHODS

Patterned ITO-coated glass substrates were cleaned with a surface-active detergent and sonicated them in acetone, methanol, and isopropanol solvents bath. Afterward, ITO substrates were dried at 120°C in an oven by 20 min followed by a UV-ozone treatment. Then, a TiO_x film was deposited on the ITO by spin coating at 6000 rpm from a TiO_x solution. Subsequently, the TiO_x films were thermally annealed at 400°C by 10 min to obtain a TiO_x layer 15 nm thick. The TiO_x solution was prepared by the sol-gel method, mixing 2-methoxyethanol, ethanolamine, and titanium (IV) isopropoxide (10:2:1 v/v). The starter reagents were vigorously stirred and heated at 120°C by 3 h. Then, the TiO_x solution was diluted in methanol (6:1 v/v). Subsequently, the PBDB-T:IT-M solution was deposited on top of the TiO_x layer by spin coating to obtain samples with different PBDB-T:IT-M layer thickness. Afterward, the PBDB-T:IT-M layers were thermally annealed at 100 or 160 °C. The PBDB-T:IT-M solution with a concentration of 20 mg/mL was prepared by dissolving the polymer and the non-fullerene in a solvent mix of chlorobenzene/1,8-diiodooctane (99.5:0.5 v/v). Finally, the samples were transferred to a vacuum chamber where 5 nm of V_2O_5 and 100 nm of Ag were thermally evaporated onto the PBDB-T:IT-M layer.

Fig. 1(a) shows the schematic of inverted polymer solar cells based on PBDB-T:IT-M and (b) the energy levels alignment of the materials in the iPSCs. The electrical properties of iPSCs were characterized by current-density vs. voltage (*J-V*) measurements using a solar simulator (Abet Technologies model 11 000 class type A, xenon arc), and a Keithley 2400 source-measure unit. The *J-V* measurements were recorded under forward-bias sweep from −1 V to 1 V. The light intensity was calibrated with a monocrystalline silicon photodiode certified by NREL at 1 sun (AM 1.5G). All the external quantum efficiency data were recorded by quantum efficiency measurement systems from Lasing, S.A. (IPCE-DC, LS1109-232), and a Newport 2936-R power-meter unit. The EQE measurements were taken under wavelength sweep from 300 nm to 800 nm. The impedance spectroscopy measurements were recorded by an HP-4192A impedance analyzer. The IS measurements were performed under AM 1.5 illumination with a frequency sweep.

III. RESULTS AND DISCUSSION
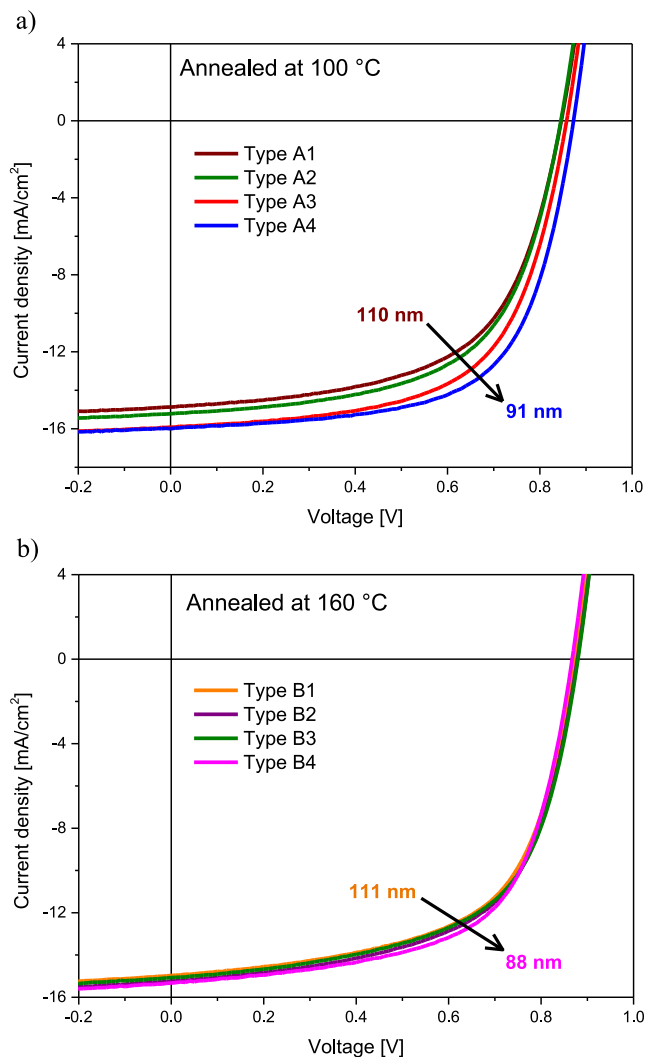
To analyze the effects of thermal annealing of PBDB-T:IT-M layer on the performance of iPSCs, we fabricated samples with temperature annealing of 100 and 160 °C labeled Type A and Type B, respectively. The effects of the different thicknesses of PBDB-T:IT-M, varying from 110 nm to 90 nm, on the performance of iPSCs were also investigated. Figs. 2 a and b show the *J-V* characteristics for
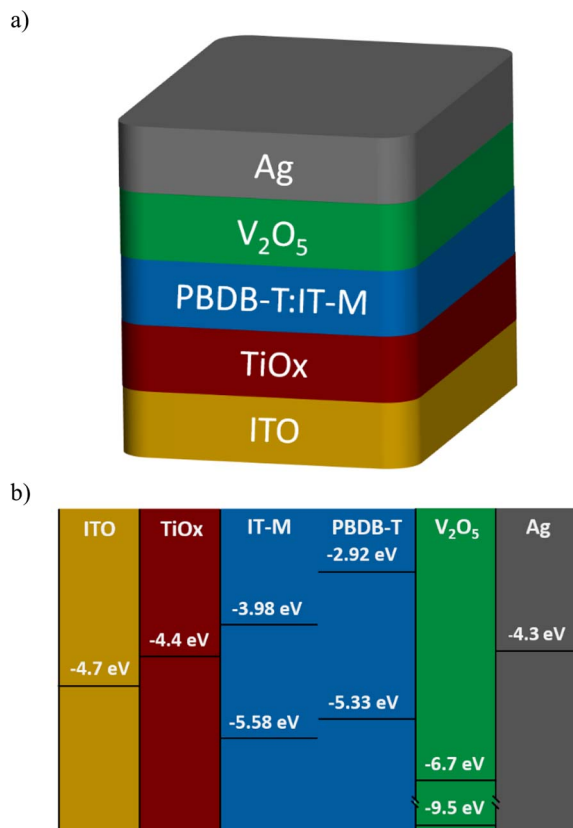
FIGURE 1. Schematic of inverted polymer solar cells based on PBDB-T:IT-M (a) and energy levels alignment of the materials in the iPSCs (b).

FIGURE 2. *J-V* characteristics for Type A (a) and Type B (b) iPSCs as a function of PBDB-T:IT-M layer thickness.

Type A and Type B iPSCs, respectively, as a function of PBDB-T:IT-M layer thickness. As shown in Fig. 2b, Type B devices show similar behavior, while the performance of Type A devices improves as the thickness of the PBDB-T:IT-M layer is decreased (see Fig. 2a). Table 1 summarizes the photovoltaic parameters, such as open-circuit voltage (V_{OC}); short-circuit current density (J_{SC}); fill factor (FF); power conversion efficiency (PCE); series resistance (R_S); and shunt resistance (R_{Sh}), for Type A and Type B devices with different active layer thickness. The values of the parameters, as well as their standard deviation, were averaged over eight devices.

The photovoltaic parameters were extracted from the *J-V* characteristics under simulated AM 1.5G solar light illumination at 1 sun. From Table 1, we notice that all photovoltaic parameters of the Type B devices are similar each to the other and the active layer thickness has not a significant effect on the device performance when it is annealed at 160°C. Nevertheless, the PCE slightly increases as the thickness of PBDB-T:IT-M layer decreases. For instance, the Type B4 device with the thinnest active layer shown highest performance (PCE of 8.28%), J_{SC} (15.32 mA/cm^2) and FF (62.12 %), but its V_{OC} (870 mV) is the lowest for iPSCs with thermal annealing of 160°C. On the other hand, for iPSCs with the PBDB-T:IT-M

film annealed at 100 °C (samples Type A) all the photovoltaic parameters improve as the active layer film thickness decreases. Samples Type A1 and Type A2 exhibit similar V_{OC}, however, sample Type A2 shows higher J_{SC} and FF than those of sample Type A1, resulting in a higher PCE (Type A2 = 7.93% and Type A1 = 7.52%). Sample Type A3 exhibits higher photovoltaic parameters than those of sample Type A2. Samples Type A3 and Type A4 exhibited similar J_{SC} ($\sim$16.10 mA/cm^2). Nevertheless, sample Type A4 has a higher FF (64.26%) than that of sample Type A3 (61.59%), resulting in higher performance for device Type A4 (PCE of 9.02%). The higher PCE is mainly due to the increase of both V_{OC} and R_{Sh}, and the low series resistance in sample Type A4. The results of Table 1 demonstrated that the best performance (9.02%) for iPSCs based on PBDB-T:IT-M can be reached by using an active layer $\sim$90 nm thick, thermally annealed at 100 °C (sample Type A4).

TABLE 1. Photovoltaic parameters of iPSCs based on PBDB-T:IT-M with different thicknesses for Type A iPSCs (annealed at 100 °C) and for Type B iPSCs (annealed at 160 °C).

Sample	Thickness [nm]	V_{OC} [mV]	J_{SC} [mA/cm^2]	FF [%]	PCE [%] Best	PCE [%] Average	R_S [Ω cm^2]	R_{Sh} [Ω cm^2]
Type A1	110	847.5±4.3	14.94±0.51	59.40±1.22	7.78	7.52±0.24	4.71±0.26	676±49
Type A2	106	845.0±7.1	15.38±0.57	60.22±0.98	8.03	7.93±0.21	4.35±0.28	756±84
Type A3	102	857.5±4.3	16.10±0.12	61.59±0.96	8.68	8.50±020	4.30±0.20	772±68
Type A4	91	870.0.±0.1	16.14±0.20	64.26±0.57	9.08	9.02±0.04	3.96±0.13	981±107
Type B1	111	872.5±4.3	15.20±0.28	60.70±0.88	8.26	8.05±0.17	4.39±0.10	617±38
Type B2	105	878.5±9.9	15.25±0.43	60.50±1.52	8.31	8.10±0.18	4.30±0.20	678±90
Type B3	100	878.7±7.8	15.18±0.35	60.50±2.00	8.46	8.07±0.26	4.12±0.16	637±60
Type B4	88	870.0±7.1	15.32±0.18	62.12±0.74	8.58	8.28±0.19	4.16±0.27	636±26

To understand the photocurrent generated in iPSCs based on PBDB-T:IT-M, we performed external quantum efficiency (EQE) measurements. EQE can be defined as the number of photogenerated carriers per incident photons. Figs. 3 a and b display the EQE spectra and the integrated J_{SC} for Type A and Type B iPSCs, respectively, as a function of PBDB-T:IT-M layer thickness. All the samples Type A and Type B exhibited similar EQE curves behavior in the wavelength region of 300-800 nm. Samples with the thinnest PBDB-T:IT-M layer showed higher EQE values (and the same intensity at 626 nm, ∼80%) than that of samples with thicker PBDB-T:IT-M layer, which is in good agreement with their higher J_{SC} shown in Fig. 2. The calculated J_{SC} values by integrating the EQE data under simulated AM 1.5G solar spectrum are 14.61, 15.15, 15.65, and 15.98 mA/cm^2 for devices Type A1, Type A2, Type A3, and Type A4, respectively. Moreover, the calculated J_{SC} values for devices Type B1, Type B2, Type B3, and Type B4 are 14.85, 15.29, 15.19, and 15.77 mA/cm^2, respectively. These results are consistent with the J_{SC} calculated from the *J-V* characteristics of Type A and Type B devices within a 4% mismatch (refer to Table 1).

To understand the charge-recombination mechanisms present in iPSCs, the dependence of both J_{SC} and V_{OC} on light intensity were analyzed. To do so, we measured *J-V* characteristics as a function of light intensity (P_{light}) as shown in Fig. 4a. The dependence of J_{SC} on the P_{light} is described as follows:
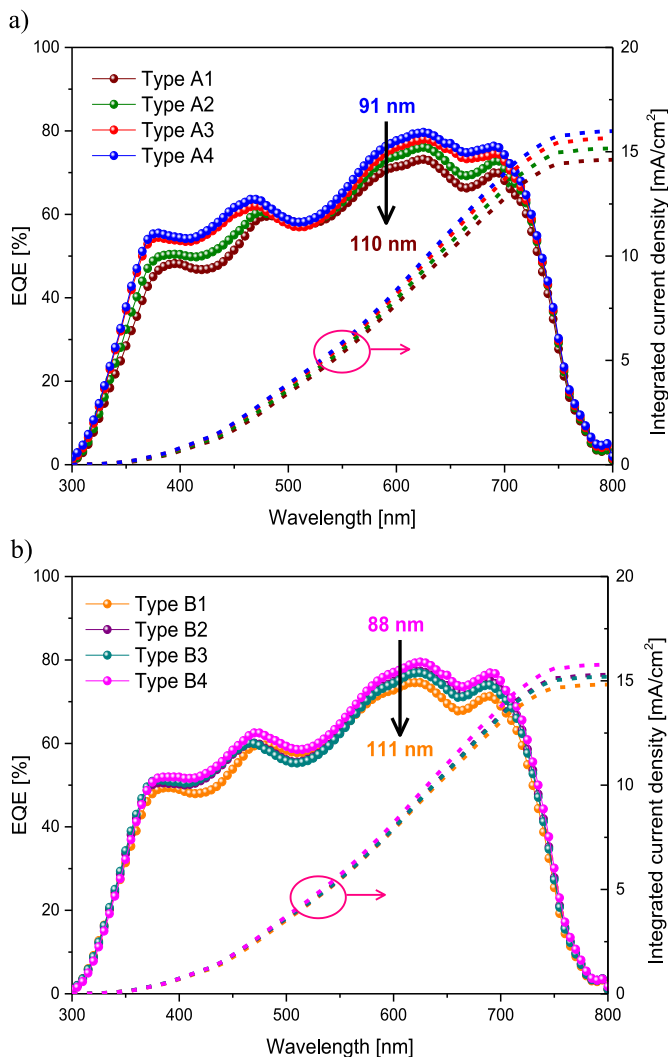
$$J_{SC} = \alpha P_{light}^{\beta}, \qquad (1)$$

where β represents the bimolecular recombination mechanism. For bulk heterojunction PSCs, the value of β is generally close to 1, which indicates weak bimolecular recombination. On the contrary, a value of β far smaller than 1 suggests bimolecular recombination of free charge carriers that limits the photocurrent of devices [35]–[37]. The plots J_{SC} versus P_{light} for Type A and Type B devices are displayed in Figs. 4b and 4c, respectively. All the plots were

fitted using equation (1). The values of β for Type A1 = 0.97, Type A2 = 1.00, Type A3 = 0.98, and Type A4 = 0.96, whereas for Type B devices the values of β are 1.00, 1.00, 0.99 and 0.99 for Type B1, B2, B3, B4 devices, respectively. These results suggest that there is not bimolecular recombination and there is not a build-up of space charge in all devices Type A and Type B. To gain more insight into recombination mechanisms in PBDB-T:IT-M based iPSCs, we calculated the ideality factor (n_{id}) of all devices by fitting the V_{OC} versus P_{light} using [38]:

$$V_{OC} = \frac{n_{id}kT}{q}ln(P_{light}) + b, \qquad (2)$$

where k is the Boltzmann constant, T is the Kelvin temperature, and q is the elementary charge. Fig. 5a displays the V_{OC} versus P_{light} plots for all the Type A iPSCs. The calculated n_{id} for devices Type A1, A2, A3, and A4 are 1.54, 1.53, 1.36 and 1.45, respectively. These results are in the range of expected values since the ideality factor for OSCs is ranged between 1 and 2 ($1 \leq n_{id} \leq 2$) [39]. It is well known that the condition of n_{id} equal to 1, indicates the bimolecular recombination mechanism governs the charge recombination in OSCs, whereas when n_{id} is near to 2, it is dominated by Schockley-Read-Hall (trap-assisted) recombination mechanism [39], [40]. The n_{id} values calculated for Type A1, A2, and A4 devices suggest the recombination losses in these samples are mainly due to band-tail trap states in the bulk. The lower n_{id} values for Type A3 and A4 can be attributed to a less concentration of traps in the bulk, resulting in higher V_{OC} values for these devices as shown in Table 1. Fig. 5b displays the V_{OC} versus P_{light} plots for all the Type B iPSCs (annealed at 160 °C), and the calculated n_{id} values are 2.73, 2.64, 2.50, and 2.49 for devices Type B1, B2, B3, and B4, respectively. The value of n_{id} decreases as the PBDB-T:IT-M film thickness is decreased. Interestingly, these ideality factor values do not satisfy the condition $1 \leq n_{id} \leq 2$. The ideality values higher than 2 can be related to the energetic disorder of organic materials due to

a)

b)

FIGURE 3. EQE spectra and integrated J_{SC} for Type A (a) and Type B (b) iPSCs as a function of PBDB-T:IT-M layer thickness.

TABLE 2. RC values of TiO_x, bulk and V_2O_5 used to fitting the IS spectra at 3 different bias voltages.

	Type A4			Type B4		
	0 V	0.55 V	0.87 V	0 V	0.55 V	0.87 V
R_{TiO_x} [Ω]	33.80	15.83	11.61	38.00	13.60	11.00
C_{TiO_x} [nF]	195	180	156	195	180	156
R_{bulk} [Ω]	44.68	36.99	39.30	21.06	24.90	26.70
C_{bulk} [nF]	5.37	4.18	4.35	5.64	4.71	4.92
$R_{V_2O_5}$ [Ω]	208	50.24	25.67	300	56.45	28.60
$C_{V_2O_5}$ [nF]	8.35	13.78	25.01	6.66	13.78	25.65
R_S [Ω]	14.75	13.97	15.94	12.78	14.13	15.80

The measurements were carried out under simulated AM 1.5 illumination in the frequency range from 10 to 1 MHz. The bias voltage was set at 0 V (short-circuit current point), at 0.55 V (close to maximum power-point), and 0.87 V (close to open-circuit point) with an oscillation amplitude of 15 mV. Figs. 6 a and b show the experimental and fitted Cole-Cole plots of the impedance spectroscopy data for Type A4 and Type B iPSCs, respectively, varying the bias voltage. Both devices exhibited the typical semicircle shape corresponding to the RC circuit at the three different bias voltages [48]. The diameter of the semicircles decreases when increasing the bias voltage in both devices. The diameter of the semicircle is directly related to the value of the resistance. Type B4 device showed higher resistance than that of Type A4 device at 0 V, however, at high bias voltage the resistance of Type A4 is slightly higher than that of Type B4 device. The IS spectra were fitted to an equivalent circuit composed of one resistance and three resistor/capacitor elements (*3RC*) in series depicted in the inset of Fig. 6a. The *RC* elements (R_iC_i; i = 1, 2 and 3) can be correlated to the different layers involved in the charge-transferring process (TiO_x, bulk, and V_2O_5), by calculating their theoretical capacitance as we report elsewhere [49]. Table 2 summarizes the values of RC elements for TiO_x, bulk, and V_2O_5 layer used to fitting the IS spectra of Type A4 and Type B4 devices at 3 different bias voltages. The capacitance of the three layers varies as the bias voltage changes, moreover, their capacitance is not affected by the annealing temperature. The resistance R_S is related to the contacts resistances, mainly due to the ITO's resistance (resistivity of ITO $\sim$10 Ω/$\square$). Device Type A4 showed higher bulk layer resistance than that of sample Type B4. The low resistance of the bulk layer of device Type B4 can
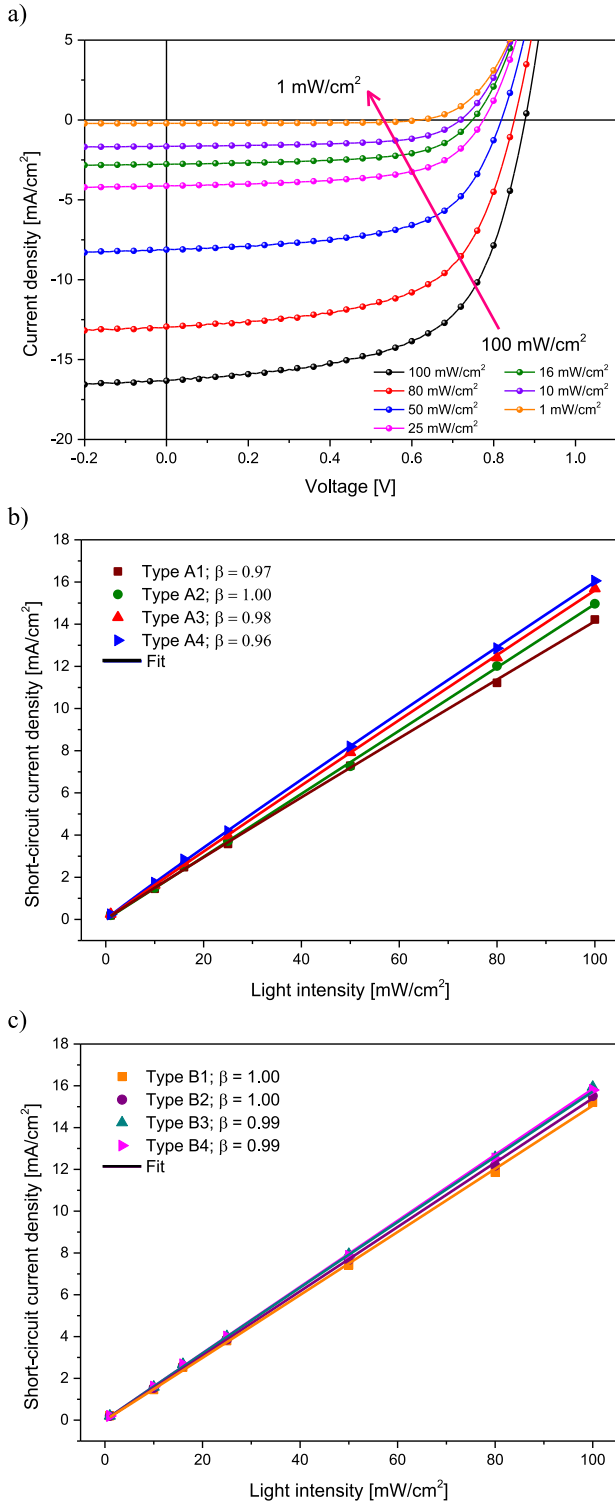
the crystallinity difference between donor and acceptor materials, which causes non-geminate recombination [41]–[43]. Li *et al.* reported a diffused donor/acceptor interface due to an increment of the PBDB-T crystallite size when the PBDB-T:IT-M layer is annealed at 160 °C [34]. The plot shows that for high light intensities range (10-100 mW/cm^2) the recombination is led by a non-geminate recombination mechanism. It has been reported non-geminate recombination can limit the FF of OSCs [44], which explains the low FF exhibited by Type B devices.

To gain an understanding of the influence of the thermal annealing temperature on the electrical properties of materials involved in the charge-transfer, we performed impedance spectroscopy (IS) measurements on Type A4 and Type B4 devices. It has been demonstrated that impedance spectroscopy is a useful method for investigating the losses and charge-transferring mechanisms involved in the charge extraction in organic solar cells [11], [45]–[47].

FIGURE 4. *J-V* characteristics as a function of light intensity (a). Experimental (symbols) and fitted (lines) J$_{SC}$ versus light intensity plot for Type A (b). Experimental (symbols) and fitted (lines) J$_{SC}$ versus light intensity plot for Type B devices (c). The fits were performed by equation (1).
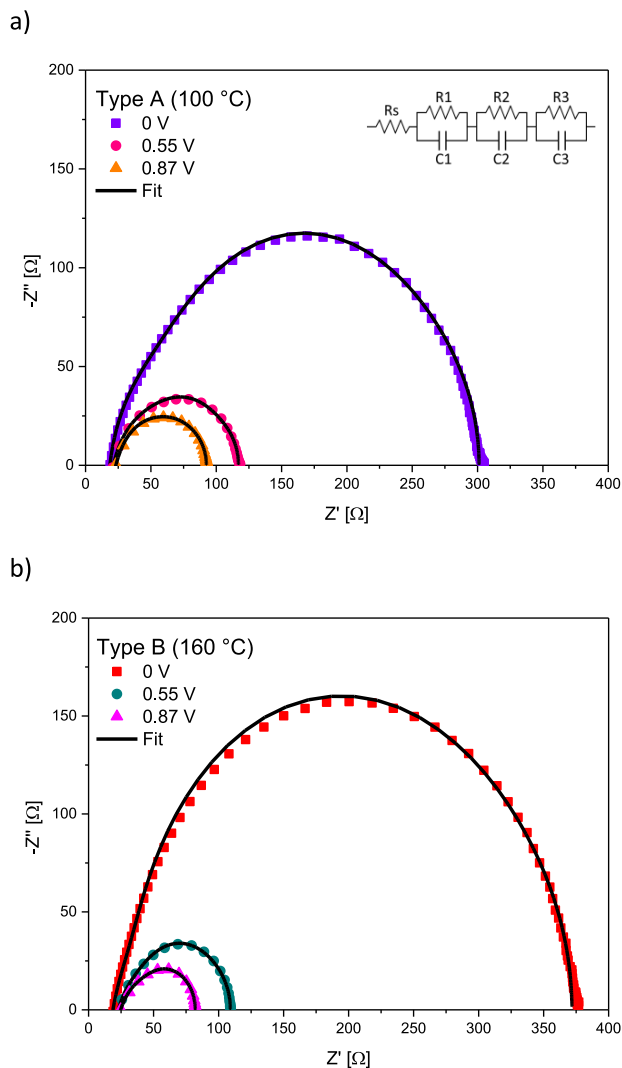

FIGURE 5. Experimental (symbols) and fitted (lines) V$_{OC}$ versus light intensity plot for Type A (a). Experimental (symbols) and fitted (lines) V$_{OC}$ versus light intensity plot for Type B devices (b). The fits were performed by equation (2).

bias voltages. This result suggests there is a charge-transfer resistance in the V_2O_5 layer at 0 V bias, which limits the short circuit current of Type B4 device.

To further analyze the influence of the thermal annealing temperature on the electrical properties of TiO_x, bulk and V_2O_5 layers we calculated the resistivity of these layers for Type A4 and Type B4. The relationship between the layers resistivities of Type B4 and Type A4 devices has been expressed as the following equation:

$$\Delta \rho_i = \frac{\rho_{B_i}}{\rho_{A_i}} = \left(\frac{R_{B_i} S_{B_i}}{d_{B_i}} \right) \left(\frac{d_{A_i}}{R_{A_i} S_{A_i}} \right) = \frac{R_{B_i}}{R_{A_i}} \quad (3)$$

where ρ is the resistivity of the layer, R is the resistance calculated from IS analysis, S is the area for each layer (0.09 cm^2 for all samples), d is the thickness of the layer (TiO_x = 15 nm, bulk = 90 nm, and V_2O_5 = 5 nm in both devices), the subscript A is for TiO_x, bulk, and V_2O_5 layers

be attributed to the enhanced electrical properties of PBDB-T:IT-M layer after annealing at 160 °C [34]. The resistance of V_2O_5 layer is higher for device Type B4 at the three

a)

b)

FIGURE 6. Experimental (symbols) and fitted (solid lines) Cole-Cole plots of the impedance spectroscopy data for Type A4 (a) and Type B4 (b) iPSCs varying the bias voltage. The equivalent circuit model used for fitting is shown inset of Fig. 6a.

TABLE 3. Relationship of layers resistivity between devices B4 and A4.

	0 V	0.55 V	0.87 V
$\Delta\rho_{TiO_x}$	1.12	0.86	0.95
$\Delta\rho_{bulk}$	0.47	0.67	0.70
$\Delta\rho_{V_2O_5}$	1.44	1.12	1.11

power point (0.55 V) Type B4 iPSC showed lower charge extraction resistance at the bulk/TiO$_x$ interface, however, it showed higher charge extraction resistance at the bulk/V$_2$O$_5$ interface. Finally, at the short-circuit current point (0 V), the charge extraction resistances at the bulk/TiO$_x$ and bulk/V$_2$O$_5$ interfaces are higher in the Type B4 device than that of Type A4 device. These results indicate the high resistances at 0V at the bulk/TiO$_x$ and bulk/V$_2$O$_5$ interfaces limit the current density of Type B4 device and are in good agreement to the lower J$_{SC}$ of Type B4 sample (see Table 1).

IV. CONCLUSION

We reported an iPSCs based on the PBDB-T polymer and the IT-M non-fullerene acceptor using TiO$_x$ as the ETL and V$_2$O$_5$ as HTL. The effects of thickness and annealing temperature of PBDB-T:IT-M layer on the performance of iPSCs were analyzed. We demonstrated iPSCs fabricated at 100 °C have a performance-dependence on the thickness of PBDB-T:IT-M, whereas this performance-dependence is less significative when the iPSCs are thermally annealed at 160 °C. The performance of iPSCs decreases when the PBDB-T:IT-M layer is thermally annealed at 160 °C. An efficiency of 9% was obtained in devices with PBDB-T:IT-M thickness of about 90 nm and thermal annealed at 100 °C. The results from the ideality factor study have brought substantial evidence that non-gemination recombination in iPSCs based on PBDB-T:IT-M is due to a thermal annealing temperature of 160 °C, which limits the FF of the device. On the other hand, the recombination mechanism is governed by band-tail trap states in the bulk when the iPSCs are annealed at 100 °C. The impedance spectroscopy measurement revealed that charge-transfer is improved at the bulk by annealing the PBDB-T:IT-M layer at 160 °C, however, the charge extraction resistance at the bulk/V$_2$O$_5$ interface is increased, limiting the short-circuit current of iPSC. Finally, IS results demonstrated that iPSCs based on PBDB-T:IT-M with an annealing temperature of 100 °C exhibited lower charge-extraction resistances, which result in more efficient devices.

REFERENCES

[1] G. Dennler, M. C. Scharber, and C. J. Brabec, "Polymer-fullerene bulk-heterojunction solar cells," *Adv. Mater.*, vol. 21, no. 13, pp. 1323–1338, 2009.

[2] G. Li, R. Zhu, and Y. Yang, "Polymer solar cells," *Nat. Photonics*, vol. 6, no. 3, pp. 153–161, 2012.

[3] A. M. Bagher, "Introduction to organic solar cells," *Sustain. Energy*, vol. 2, no. 3, pp. 85–90, 2014.

of Type A4 device, and subscript B is for those of Type B4 device, and i = TiO$_x$, bulk or V$_2$O$_5$ layer. The values of the relationship between resistivity of layers the devices Type B4 and Type A at three bias voltages are summarized in Table 3. The $\Delta\rho_{bulk}$ in Type B4 device is ~50% (at 0V), and ~30% (at high bias voltages) lower in comparison to that in device Type A4. The $\Delta\rho_{TiO_x}$ in Type B4 device is lower (up to 14 %) than that of device Type A4 at high bias voltages. On the other hand, the $\Delta\rho_{TiO_x}$ in Type B4 device is 12 % higher than that of Type A4 at 0 V. The $\Delta\rho_{V_2O_5}$ of Type B4 device is 44% higher at 0 V, and ~11% higher at high bias voltages in comparison to that of device Type A4. These results demonstrate that the charge transfer in the bulk is better in Type B4 device in comparison to Type A4 device. Close to the V$_{OC}$ point (0.87 V), the charge-extraction resistances at the bulk/TiO$_x$ and bulk/V$_2$O$_5$ interfaces are similar for both devices. Moreover, close to the maximum

[4] Y. Liang and L. Yu, "A new class of semiconducting polymers for bulk heterojunction solar cells with exceptionally high performance," *Acc. Chem. Res.*, vol. 43, no. 9, pp. 1227–1236, 2010.

[5] Y. Liang *et al.*, "Highly efficient solar cell polymers developed via fine-tuning of structural and electronic properties," *J. Amer. Chem. Soc.*, vol. 131, no. 22, pp. 7792–7799, 2009.

[6] P. Han *et al.*, "Improving the efficiency of PTB1: PCBM bulk heterojunction solar cells by polymer blend solution aging," *IEEE J. Photovolt.*, vol. 5, no. 3, pp. 889–896, May 2015.

[7] Y. Liang *et al.*, "For the bright future-bulk heterojunction polymer solar cells with power conversion efficiency of 7.4%," *Adv. Mater.*, vol. 22, no. 20, pp. 135–138, 2010.

[8] K. Sun *et al.*, "Review on application of PEDOTs and PEDOT: PSS in energy conversion and storage devices," *J. Mater. Sci. Mater. Electron.*, vol. 26, pp. 4438–4462, Mar. 2015.

[9] V. S. Balderrama *et al.*, "Degradation of electrical properties of PTB1:PCBM solar cells under different environments," *Solar Energy Mater. Solar Cells*, vol. 125, pp. 155–163, Jun. 2014.

[10] M. Jørgensen, K. Norrman, S. A. Gevorgyan, T. Tromholt, B. Andreasen, and F. C. Krebs, "Stability of polymer solar cells," *Adv. Mater.*, vol. 24, no. 5, pp. 580–612, 2012.

[11] B. Ecker *et al.*, "Degradation effects related to the hole transport layer in organic solar cells," *Adv. Funct. Mater.*, vol. 21, no. 14, pp. 2705–2711, 2011.

[12] M. Jørgensen, K. Norrman, and F. C. Krebs, "Stability/degradation of polymer solar cells," *Solar Energy Mater. Solar Cells*, vol. 92, no. 7, pp. 686–714, 2008.

[13] J. G. Sánchez *et al.*, "Stability study of high efficiency polymer solar cells using TiO$_x$ as electron transport layer," *Solar Energy*, vol. 150, pp. 147–155, Jul. 2017.

[14] G. Kim *et al.*, "Overcoming the light-soaking problem in inverted polymer solar cells by introducing a heavily doped titanium sub-oxide functional layer," *Adv. Energy Mater.*, vol. 5, no. 3, pp. 21–23, 2015.

[15] B. Xiao, H. Wu, and Y. Cao, "Solution-processed cathode interfacial layer materials for high-efficiency polymer solar cells," *Mater. Today*, vol. 18, no. 7, pp. 385–394, 2015.

[16] Z. Liang, Q. Zhang, L. Jiang, and G. Cao, "ZnO cathode buffer layers for inverted polymer solar cells," *Energy Environ. Sci.*, vol. 8, no. 12, pp. 3442–3476, 2015.

[17] J. G. Sánchez *et al.*, "Impact of inkjet printed ZnO electron transport layer on the characteristics of polymer solar cells," *RSC Adv.*, vol. 8, no. 24, pp. 13094–13102, 2018.

[18] Z. He, C. Zhong, S. Su, M. Xu, H. Wu, and Y. Cao, "Enhanced power-conversion efficiency in polymer solar cells using an inverted device structure," *Nat. Photonics*, vol. 6, no. 9, pp. 593–597, 2012.

[19] V. S. Balderrama *et al.*, "High-efficiency organic solar cells based on a halide salt and polyfluorene polymer with a high alignment-level of the cathode selective contact," *J. Mater. Chem. A*, vol. 6, no. 45, pp. 22534–22544, 2018.

[20] J. Meyer, S. Hamwi, M. Kröger, W. Kowalsky, T. Riedl, and A. Kahn, "Transition metal oxides for organic electronics: Energetics, device physics and applications," *Adv. Mater.*, vol. 24, no. 40, pp. 5408–5427, 2012.

[21] Z. He *et al.*, "Single-junction polymer solar cells with high efficiency and photovoltage," *Nat. Photonics*, vol. 9, no. 3, pp. 174–179, 2015.

[22] P. Cheng, G. Li, X. Zhan, and Y. Yang, "Next-generation organic photovoltaics based on non-fullerene acceptors," *Nat. Photonics*, vol. 12, no. 3, pp. 131–142, 2018.

[23] S. Li *et al.*, "A wide band gap polymer with a deep highest occupied molecular orbital level enables 14.2% efficiency in polymer solar cells," *J. Amer. Chem. Soc.*, vol. 140, no. 23, pp. 7159–7167, 2018.

[24] A. Wadsworth *et al.*, "Critical review of the molecular design progress in non-fullerene electron acceptors towards commercially viable organic solar cells," *Chem. Soc. Rev.*, vol. 48, no. 6, pp. 1596–1625, 2019.

[25] C. Yan *et al.*, "Non-fullerene acceptors for organic solar cells," *Nat. Rev. Mater.*, vol. 3, no. 3, Feb. 2018, Art. no. 18003.

[26] J. Zhang, H. S. Tan, X. Guo, A. Facchetti, and H. Yan, "Material insights and challenges for non-fullerene organic solar cells based on small molecular acceptors," *Nat. Energy*, vol. 3, no. 9, pp. 720–731, 2018.

[27] H. Choi *et al.*, "Efficiency enhancements in non-fullerene acceptor-based organic solar cells by post-additive soaking," *J. Mater. Chem. A*, vol. 7, no. 15, pp. 8805–8810, 2019.

[28] S. Li *et al.*, "Energy-level modulation of small-molecule electron acceptors to achieve over 12% efficiency in polymer solar cells," *Adv. Mater.*, vol. 28, no. 42, pp. 9423–9429, 2016.

[29] W. Zhao *et al.*, "Fullerene-free polymer solar cells with over 11% efficiency and excellent thermal stability," *Adv. Mater.*, vol. 28, no. 23, pp. 4734–4739, 2016.

[30] W. Zhao *et al.*, "Molecular optimization enables over 13% efficiency in organic solar cells," *J. Amer. Chem. Soc.*, vol. 139, no. 21, pp. 7148–7151, 2017.

[31] Z. Li *et al.*, "Donor polymer design enables efficient non-fullerene organic solar cells," *Nat. Commun.*, vol. 7, no. 9, pp. 1–9, 2016.

[32] H. You, L. Dai, Q. Zhang, D. Chen, Q. Jiang, and C. Zhang, "Enhanced performance of inverted non-fullerene organic solar cells by using metal oxide electron-and hole-selective layers with process temperature ≤150 °C," *Polymers*, vol. 10, no. 7, p. 725, 2018.

[33] Q. An *et al.*, "High-efficiency and air stable fullerene-free ternary organic solar cells," *Nano Energy*, vol. 45, pp. 177–183, Mar. 2018.

[34] W. Li *et al.*, "Correlating three-dimensional morphology with function in PBDB-T:IT-M non-fullerene organic solar cells," *Solar RRL*, vol. 2, no. 9, 2018, Art. no. 1870204.

[35] I. Riedel, J. Parisi, V. Dyakonov, L. J. Lutsen, D. Vanderzande, and J. C. Hummelen, "Effect of temperature and illumination on the electrical characteristics of polymer-fullerene bulk-heterojunction solar cells," *Adv. Funct. Mater.*, vol. 14, no. 1, pp. 38–44, 2004.

[36] D. Credgington, Y. Kim, J. Labram, T. D. Anthopoulos, and J. R. Durrant, "Analysis of recombination losses in a pentacene/C60 organic bilayer solar cell," *J. Phys. Chem. Lett.*, vol. 2, pp. 2759–2763, 2011.

[37] L. J. A. Koster, M. Kemerink, M. M. Wienk, K. Maturová, and R. A. J. Janssen, "Quantifying bimolecular recombination losses in organic bulk heterojunction solar cells," *Adv. Mater.*, vol. 23, no. 14, pp. 1670–1674, 2011.

[38] L. J. A. Koster, V. D. Mihailetchi, R. Ramaker, and P. W. M. Blom, "Light intensity dependence of open-circuit voltage of polymer: Fullerene solar cells," *Appl. Phys. Lett.*, vol. 86, no. 12, pp. 1–3, 2005.

[39] T. Kirchartz and J. Nelson, "Meaning of reaction orders in polymer: Fullerene solar cells," *Phys. Rev. B, Condens. Matter*, vol. 86, no. 16, pp. 1–12, 2012.

[40] S. R. Cowan, A. Roy, and A. J. Heeger, "Recombination in polymer-fullerene bulk heterojunction solar cells," *Phys. Rev. B, Condens. Matter*, vol. 82, no. 24, pp. 1–10, 2010.

[41] C. Xiong, J. Sun, H. Yang, and H. Jiang, "Real reason for high ideality factor in organic solar cells: Energy disorder," *Solar Energy*, vol. 178, pp. 193–200, Jan. 2019.

[42] G. Garcia-Belmonte, "Carrier recombination flux in bulk heterojunction polymer: Fullerene solar cells: Effect of energy disorder on ideality factor," *Solid-State Electron.*, vol. 79, pp. 201–205, Jan. 2013.

[43] Z.-H. Chen *et al.*, "Quantitatively characterized crystallization effect on recombination energy loss in non-fullerene organic solar cells," *J. Phys. Chem. C*, vol. 123, no. 20, pp. 12676–12683, 2019.

[44] R. Mauer, I. A. Howard, and F. Laquai, "Effect of nongeminate recombination on fill factor in polythiophene/methanofullerene organic solar cells," *J. Phys. Chem. Lett.*, vol. 1, no. 24, pp. 3500–3505, 2010.

[45] B. Ecker, H.-J. Egelhaaf, R. Steim, J. Parisi, and E. Von Hauff, "Understanding S-shaped current–voltage characteristics in organic solar cells containing a TiO$_x$ interlayer with impedance spectroscopy and equivalent circuit analysis," *J. Phys. Chem. C*, vol. 116, no. 31, pp. 16333–16337, 2012.

[46] B. Arredondo, M. B. Martín-López, B. Romero, R. Vergaz, P. Romero-Gomez, and J. Martorell, "Monitoring degradation mechanisms in PTB7: PC$_{71}$BM photovoltaic cells by means of impedance spectroscopy," *Solar Energy Mater. Solar Cells*, vol. 144, pp. 422–428, Jan. 2016.

[47] G. Garcia-Belmonte, P. P. Boix, J. Bisquert, M. Sessolo, and H. J. Bolink, "Simultaneous determination of carrier lifetime and electron density-of-states in P3HT: PCBM organic solar cells under illumination by impedance spectroscopy," *Solar Energy Mater. Solar Cells*, vol. 94, no. 2, pp. 366–375, 2010.

[48] M. S. Suresh, "Measurement of solar cell parameters using impedance spectroscopy," *Solar Energy Mater. Solar Cells*, vol. 43, no. 1, pp. 21–28, 1996.

[49] E. Osorio *et al.*, "Degradation analysis of encapsulated and nonencapsulated TiO$_2$/PTB7: PC$_{70}$BM/V$_2$O$_5$ solar cells under ambient conditions via impedance spectroscopy," *ACS Omega*, vol. 2, no. 7, pp. 3091–3097, 2017.